

A New Registration Approach for Wing Pouch Image Sequence Analysis

Peixian Liang^{*§}, Jianxu Chen^{*§}, Pavel A. Brodskiy[†], Qinfeng Wu[†], Yejia Zhang[‡], Yizhe Zhang^{*}, Lin Yang^{*}, Jeremiah J. Zartman[†], Danny Z. Chen^{*}

^{*}Department of Computer Science and Engineering, University of Notre Dame, Notre Dame, IN 46556, USA

[†]Department of Chemical and Biomolecular Engineering, University of Notre Dame, Notre Dame, IN 46556, USA

[‡]Department of Electrical and Computer Engineering, University of California San Diego, CA 92093, USA

Abstract—Wing pouches of fruit flies are a powerful genetic model system that has been used widely for studying the conserved biological functions related to intercellular calcium (Ca^{2+}) signaling. Quantitative analyses of the spatial-temporal patterns of Ca^{2+} signal waves can provide valuable information for organ development and disease studies. Due to the nature of live imaging, the same wing pouch captured at different frames of an image sequence may incur considerable movement. As a result, registration, namely, accurately aligning the wing pouches across the whole image sequence, becomes a crucial step for Ca^{2+} spatial-temporal analysis. Since wing pouches in different image frames exhibit extensive intensity oscillations due to Ca^{2+} signaling dynamics, commonly used multimodal non-rigid registration methods fail to achieve satisfactory results. In this paper, we develop a new two-phase non-rigid registration approach to automatically register wing pouches in image sequences. First, we conduct segmentation of the region of interest (i.e., wing pouches) using a deep neural network, followed by a boundary refinement post processing. Second, we apply B-spline based registration to obtain an optimal transformation and align wing pouches across the whole image sequence. Evaluated using both synthetic data and real wing pouch data, our method considerably outperforms the state-of-the-art non-rigid registration algorithms and achieves good quality results for wing pouch image sequence analysis.

I. INTRODUCTION

Ca^{2+} is a ubiquitous second messenger in organisms [1], [2]. Quantitatively analyzing spatial-temporal patterns of intercellular calcium (Ca^{2+}) signaling in tissues is important for understanding certain biological functions (e.g., the regulation of cell proliferation, metabolism, and death) and disease studies (e.g., Alzheimer's disease [3] and metastatic cancers [4]). The wing pouches of fruit flies, as a well-known genetic model system, are widely used in the study of decoding Ca^{2+} signaling [1], [2].

To quantify Ca^{2+} signaling dynamics, we need to extract spatial-temporal patterns of Ca^{2+} signatures from each pouch and create composite maps of cellular signaling over time. However, considerable movement may occur to the live organ during the whole imaging period. In this scenario, an effective automatic registration approach for wing pouches is needed.

Registering wing pouches in image sequences is a challenging problem for the following reasons. Wing pouches at different time points are moving or deforming due to a general feature of tissue growth, morphogenesis (see Fig. 1).

Furthermore, an image movie can contain many frames, and a number of movies are used to generate composite maps, which make the processing more complicated and costly. Due to intricate deformations in wing pouches, the registration problem cannot be solved by optimal rigid or affine transformations, and more sophisticated non-rigid registration is needed. Lots of research have been done on non-rigid medical image registration. Intensity-based approaches are an important technique for non-rigid registration problems, whose basic principle is to maximize a criterion measuring the intensity similarity between images. B-spline free-form deformation (FFD) is a widely used non-rigid registration method to characterize deformation using a grid of control points, but the most common similarity measures are based on the assumption of spatial independence [5]. However, the intensity inside the wing pouches may change frequently due to dynamic Ca^{2+} signal waves. Consequently, these intensity-based registration methods may fail.

To deal with the cumbersome intensity distortion, multimodal non-rigid registration has been applied. A mutual information similarity measure that does not assume the relationship between corresponding pixel intensities lent it applicable to multimodality images [6]. However, it works only for limited cases and does not perform well when two images are very different. A method for minimizing the error residual between the local phase-coherence representations of two images was proposed to deal with non-homogeneity in images [7], which relies heavily on structural information. However, in our problem, the intensity inside the wing pouches changes a lot, thus causing these methods to fail. A Markov-Gibbs random field model with pairwise interaction was presented to learn prior appearance of a given prototype, which makes it possible to align complex images [8]. But, its performance is limited and it is time-consuming. Incorporation of spatial and geometric information was proposed to address the limitations of the static local intensity relationship [9]. However, it incurs very high computation cost and cannot be applied to large-size images. In our problem, one wing pouch image sequence may have hundreds of frames, and hundreds of sequences are used to compute composite maps for cellular signaling. Hence, these methods do not work well for our problem. In general, known methods do not address well the kind of complex intensity distortion in our images with a reasonable computation cost.

In addition, we need to deal with the segmentation problem. It is not easy to detect the ROI (i.e., wing pouches), since other

[§]These authors contribute equally to this work.

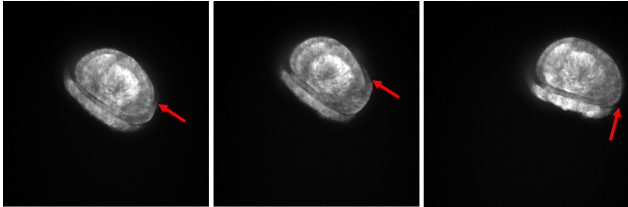


Fig. 1: Illustrating deformations and movements of wing pouches in an image sequence. The same pouch at different time points in the same image sequence is shown. The deformation parts are pointed to by red arrows.

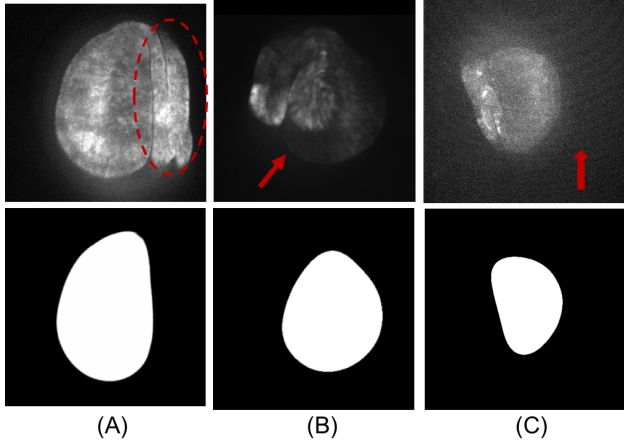


Fig. 2: Some difficult cases for the detection of real pouches. The top row gives some raw images; the bottom row gives real wing pouches. (A) Some connected non-pouch tissues are marked by a red circle. (B) A red arrow points to a blurry boundary. (C) A red arrow points to a noisy region.

signals often interfere with ROI identification (see Fig. 2). For example, there are other tightly connected tissues which look similar to the pouches in intensity and texture. Also, many wing pouches have blurry boundaries and inevitable noise due to technical causes. Thus, it is a non-trivial task to accurately segment and register wing pouch image sequences.

To address the difficulty of spatial intensity distortion along with various ROI deformations and movements, we propose a new non-rigid registration approach to effectively align wing pouches at different time points. Our approach consists of two main stages: (1) a segmentation stage and (2) a mapping stage (see Fig. 3). The segmentation stage is achieved using a deep neural network (DNN) [10]. Because the accuracy of the boundary is a key factor influencing the registration results, we apply a graph search algorithm to refine the segmented pouch boundaries. The mapping stage uses the segmentation results from the first stage to characterize an optimal transformation. We first apply a rigid transformation to modulate the movement of wing pouches, and then design an object pre-detection B-spline based non-rigid algorithm to produce the final mapping.

Our experiments use 8 movies with totally 160 synthetic images and 8 movies with 100 real wing pouch images to evaluate and compare the performance of different registration methods. The experiments show that our method outperforms

the state-of-the-art multimodal non-rigid registration methods on both synthetic images and real data. It also shows that the mapping method we design is better than other methods. Furthermore, the results of the segmentation part show that traditional segmentation methods are inadequate to our problem, and our DNN and boundary refinement are more effective. Comparing to previous multimodal non-rigid registration methods, our approach can achieve better registration results on image sequences where intensity distortions are prevalent.

II. METHODOLOGY

Our registration approach mainly consists of two stages. An overview of our approach is given in Fig. 3. The first stage segments the wing pouch in each image frame by a DNN model and refines the segmented pouch boundary by a graph search algorithm. The second (mapping) stage has two steps: (i) a rigid transformation is applied to roughly align the shapes; (ii) a B-spline based model is employed to characterize an optimal deformation and determine the final registration.

A. Segmentation Stage

Accurate segmentation of the wing pouches is a foundation of success to our proposed registration approach. Wing pouches in our images are commonly surrounded and touched by extra tissues with similar intensity and texture, and the separation boundary between the pouches and extra tissues is usually of poor visibility (see Fig. 2(A)-(B)). Meanwhile, the noise induced by the live imaging process (see Fig. 2(C)) makes the segmentation task more challenging. Thus, it is important for our segmentation algorithm to leverage the morphological and topological contexts, in order to correctly segment the shape of each actual wing pouch, especially its boundary, from the noisy background. For this, we employ an FCN model to exploit the semantic context for accurate segmentation and a graph search algorithm to further refine the boundaries.

1) FCN module: Recently, deep learning methods have emerged as a powerful tool for semantic segmentation. Fully convolutional networks (FCN) have been widely used in general semantic segmentation [11] and biomedical image segmentation [12], [13], [14].

It is worth mentioning that in our images, the separation boundary between a wing pouch and other tissues is usually quite subtle (as thin as 3 to 5 pixels wide) and obscure, while the whole contextual region (including both the wing pouch and extra tissues) can be of a relatively large scale (more than 200×200 pixels). Therefore, the FCN model must fully exploit both the fine details and a very large context. For this purpose, we carefully design the FCN architecture following the model in [10] to leverage a large receptive field without sacrificing model simplicity and neglecting fine details. The exact structure of our FCN model is depicted in Fig. 4. Our model is more effective in dealing with noisy images and blurring shape boundaries than commonly used FCN models for biomedical image segmentation such as U-net [14] and CUMedNet [12], which will be shown in Section III.A.

Contrast enhancement [15] is applied at both the training process and inference process to pre-process the images before feeding them to our FCN model. More details on the model training will be presented in Section III.A.

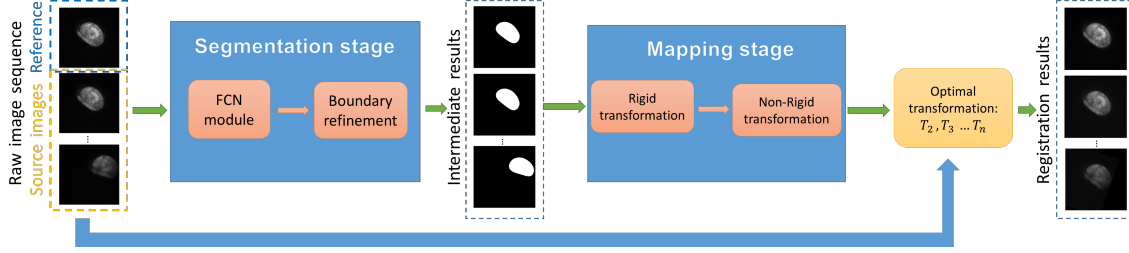


Fig. 3: An overview of our proposed registration approach.

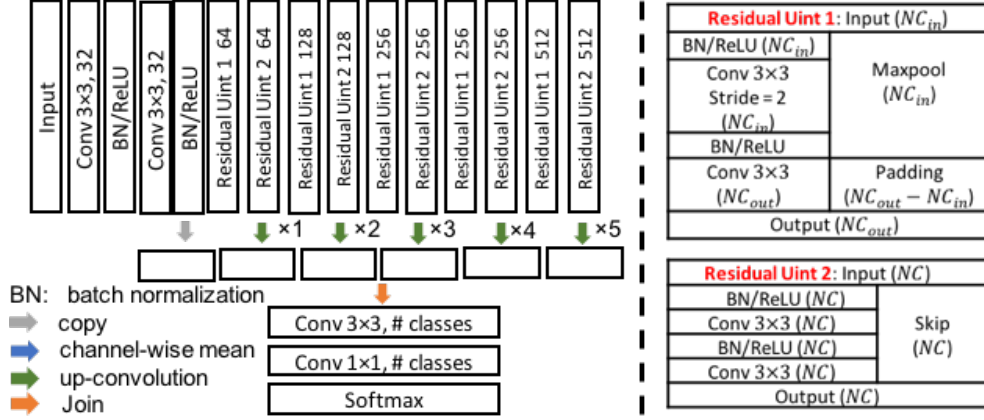


Fig. 4: The structure of our DNN model.

2) *Boundary refinement*: We observed that the boundaries of the output wing pouches from our DNN model may be fuzzy or of irregular shape in difficult cases (see Fig. 8(F)). To improve the boundary accuracy of the segmented wing pouches, we employ a graph search algorithm to further refine the shape boundaries. This will allow the subsequent mapping stage to be built upon more accurate segmentation and produce better registration results.

For a segmented region P obtained by the DNN model, we aim to refine P 's boundary contour C to C' , such that the enclosed region of C' , say P' , captures the target wing pouch more accurately. Since wing pouches usually have smooth and near convex shapes, we impose a smoothness constraint and a (near) convex-shape constraint in computing C' from C .

We model this optimal contour refinement problem as a shortest path problem on a graph. Given a contour C , we first sample uniformly g points along C clockwise. For each sample point a , we draw a ray r_a of h pixels orthogonal to the direction of the curvature of C at a (r_a centers at $a \in C$). The i -th sample point (pixel) on the j -th ray is denoted by p_i^j , i.e., $p_i^j = (x_{p_i^j}, y_{p_i^j})$ is a 2D point in the image domain. To enforce the smoothness constraint specified by a smoothness parameter s , each p_i^j is allowed to connect only to points $p_{i'}^{j+1-\lfloor j/g \rfloor \times g}$ for the sought contour C' , for $|i' - i| \leq s$, $i = 1, 2, \dots, h$, $i' = 1, 2, \dots, h$, and $j = 1, 2, \dots, g$. To enforce the (near) convex-shape constraint, any concave edge-to-edge connection ($p_i^{j-1} p_i^j$ to $p_{i'}^j p_{i''}^{j+1}$) along C' is penalized by having a large connection cost. Note that if this connection cost is $+\infty$, then

C' is a convex shape; otherwise, C' can be near convex.

A graph G is then built on all the sample points with the weights of the negatives of the gradients. Since there are lots of intensity variations inside the pouches in our images, we first apply a Gaussian smooth filter to reduce their influences on the possible edges (see Fig. 5). Wing pouches are near convex-shape objects in the image sequences, which means that the points on the refined wing pouch boundaries should form near convex shapes. Thus, we use the degree cost penalty as edge weights in G to enforce each refined pouch as a (near) convex shape.

Computing a shortest path in the graph G (using a dynamic programming algorithm in polynomial time) provides an optimal contour C' obtained from contour C subject to the two constraints above. We take C' as the sought ROI shape boundary, i.e., the final output of our segmentation stage.

B. Mapping Stage

The goal of the registration process is to obtain the optimal corresponding point in the reference image for every point in the source images. A key observation is that the intensity profile of the same wing pouch may incur substantial changes in different frames of an image sequence, due to undergoing Ca^{2+} wave signaling. Hence, intensity is not a reliable cue for finding optimal correspondence between points in different frames of a sequence.

Here, we utilize the results from the segmentation stage. First, we apply a rigid transformation to the segmentation

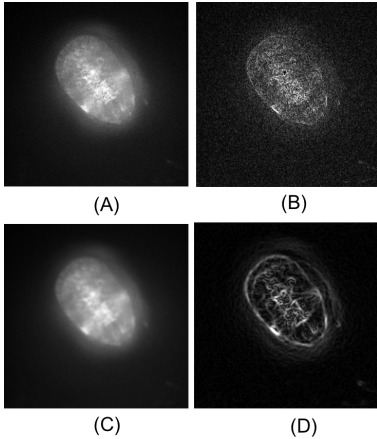


Fig. 5: Illustrating the effect of Gaussian smoothing for constructing a gradient-based cost function in our graph search algorithm. (A) A raw image. (B) The image of (A) after applying the Sobel edge detector. (C) The image of (A) after applying the Gaussian filter with radius 2.50. (D) The image after applying the Sobel edge detector to the image in (C).

results to roughly align the source and reference images. After that, we crop a sub-region from the raw images to perform B-spline free-form deformation (FFD). We take the reference image as the first frame of the sequence, while the remaining images in the sequence are treated as source images for registration, one at a time, so that every frame of the whole sequence can be aligned according to the first frame at the end.

1) Rigid transformation: Rigid transformation maintains the size and shape of an object. We compute an optimal transformation using regular-step gradient descent optimization. Note that here, local optimum traps could be an issue in practice. Specifically, since the wing pouches are often of oval shapes, a local optimum may yield incorrect results where the object is aligned with the opposite orientation (see Fig. 6). To resolve this issue, we always initialize the optimization process using the optimum parameters computed from the preceding frame in the sequence, since the wing pouch movement in consecutive frames is usually not big.

2) Non-rigid transformation: The goal of non-rigid registration is to obtain an optimal transformation $T: (x, y, t) \rightarrow (x', y', t_0)$, which maps any points on the source images at time t to time t_0 (i.e., in the reference image). We use the free-form deformation (FFD) transformation model, based on B-splines [16], to find an optimal transformation. The basic idea of FFD is to manipulate a mesh of control points to deform the objects. B-spline is a powerful tool to produce a smooth and continuous C^2 transformation [17], in which changing one control point only affects the transformation in a local neighborhood of the manipulated control points.

Not too many control points are needed outside a wing pouch, because we are concerned only with the ROI. Thus, detecting ROIs first can save computation time. Wing pouches will be near the same position after the rigid registration, which makes it possible to do non-rigid transformation only around the ROI area. Based on this observation, we can crop an area in the first frame, and then apply a lattice Φ to this area in

the following changing images. We define the lattice Φ as an $(m+3) \times (n+3)$ grid in the domain Ω (see Fig. 7).

We define the model as follows: Let $\Omega = \{(x, y) \mid X_{left} \leq x < X_{right}, Y_{left} \leq y < Y_{right}\}$ be a rectangular domain in the xy plane, where X and Y specify the boundary of the detection area. To approximate the intensity of scattered points, $I(x, y)$, in a wing pouch, we formulate a function f as a uniform cubic B-spline function:

$$f(x, y) = \sum_{j=0}^3 \sum_{i=0}^3 B_i(s) B_j(t) \Phi_{(i+k, j+l)}$$

where $s = x - \lfloor x \rfloor$, $t = y - \lfloor y \rfloor$, $k = \lfloor x \rfloor - 1$, and $l = \lfloor y \rfloor - 1$. In addition, B_i represents the i -th basis function of the cubic B-spline:

$$\begin{aligned} B_0(t) &= (1-t)^3/6, \\ B_1(t) &= (3t^3 - 6t^2 + 4)/6, \\ B_2(t) &= (-3t^3 - 6t^2 + 4)/6, \\ B_3(t) &= (t^3)/6. \end{aligned}$$

Since the resolution of the control points determines the non-rigid degree and has a big impact on the computation time, a higher resolution of control points gives more freedom to do deformation while also increasing the computation time. To optimize this trade-off, we use a multi-level mesh grid approach [18] to devise a computationally efficient algorithm.

Let $\Phi_1, \Phi_2, \dots, \Phi_n$ denote a hierarchy of meshes of control points with increasing resolutions and T_1, T_2, \dots, T_n be the deformation functions with respect to each mesh. We first apply a coarse deformation, and then refine the deformation gradually. The size of the mesh grid is increased by a power of 2 with the same spacing, so that the raw image is down sampled to the corresponding size at different levels. The final deformation is the composition of these functions:

$$T(\Omega) = T_n(\dots T_2(T_1(\Omega))\dots)$$

To obtain an optimal transformation Φ , we minimize the following energy function:

$$E = C_{similarity}(I(t_0, T(I(t)))) + QS$$

where the first term is the similarity measure and the second term is for regularization. Q is the curvature penalization and S is the displacement of the control points. The similarity measure that we adopt is the sum of squared distance (SSD):

$$SSD = \frac{1}{n} \sqrt{\sum I(t_0 - T(I(t)))^2}$$

This process iteratively updates the transformation parameters, T , using a gradient descent algorithm which steps in the direction of the gradient vector with an initial step size μ and a multiplicative constant λ . If the step size is too big and the energy function does not decrease during an iteration, then we

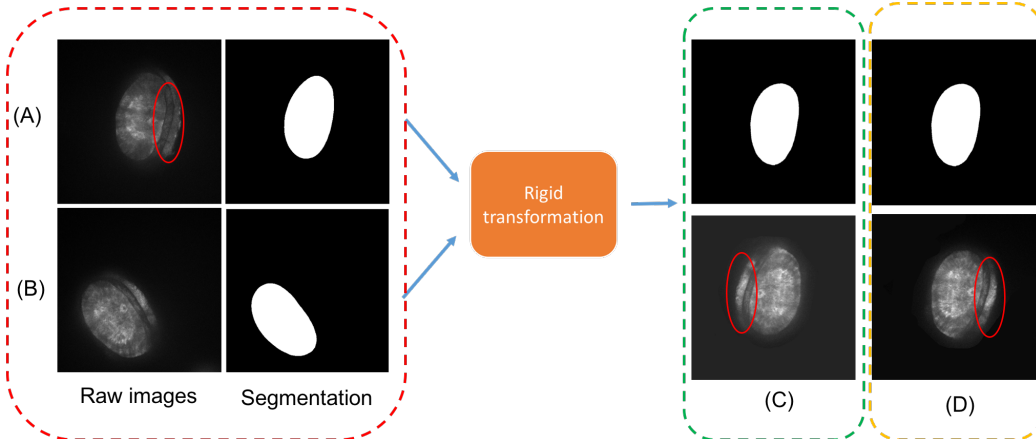


Fig. 6: An incorrect alignment example. (A) A reference image with segmentation. (B) A source image with segmentation. (C) An incorrect alignment result (a red circle marks some extra tissues, which should be on the right). (D) The expected alignment.

update $\mu = \mu \times \lambda$. When a local optimum of the cost function is smaller than ϵ or the number of iterations is bigger than N , the algorithm will terminate.

III. EXPERIMENTS AND EVALUATIONS

We evaluate our registration approach from two perspectives. First, we evaluate the accuracy of our segmentation method and compare with other common biomedical image segmentation methods, because the segmentation accuracy is crucial to our overall approach. Second, we conduct experiments using both synthetic data and real biological data to assess the registration performance of different approaches.

A. Segmentation Evaluations

The shapes and intensity profiles of wing pouches exhibit large variations from image to image in sequences. Hence, we conduct extensive segmentation evaluation, while comparing with both traditional methods (e.g., level set [19]) and state-of-the-art FCN models (i.e., U-Net [14] and CUMedNet [12]).

To evaluate our DNN model for segmenting wing pouches, we apply it to wing pouches obtained from the Bloomington Drosophila Stock Center. The training dataset consists of 800 images selected from the first time point of each video. The testing data contain 100 images selected from 10 randomly chosen control videos (300 seconds between two consecutive frames). All testing data are excluded from the training set.

The FCN models (including our model, U-net, and CUMedNet) are implemented in Torch (<http://torch.ch/>) and trained on a TITAN X GPU (12 GB graphics memory). The optimizer is Adam [20] with a learning rate of 0.0005. Data augmentation (random rotation and flip) is used during training. All the images used in the experiments are pre-processed by enhancing contrast with a saturation of 0.3%. We use the mean IU (intersection over union) and F1 as the metrics.

Table I shows the quantitative results of different methods, and Fig. 8 shows some segmentation examples of a wing pouch using different methods. The classic level-set method does not perform very well on this problem, due to complex

	Mean IU	F1 score
Level set	0.8235	0.8294
CUMedNet	0.9394	0.9454
U-net	0.9479	0.9542
Our DNN	0.9586	0.9643
Our DNN + BR	0.9617	0.9682

TABLE I: Comparison results of segmentation.

intensity profiles within wing pouches and obscure boundaries. For common FCN models such as U-net and CUMedNet, despite their high accuracy, their performance on complicated wing pouch images is still not very good. When a wing pouch is interfered considerably by other signals, these FCN models do not segment the correct ROI and cannot generate smooth boundary. Fig. 8 shows that our DNN model is better in segmenting difficult ROIs, and Fig. 8(g) shows that our boundary refinement can help obtain convex objects.

B. Registration Results

In the experiments for registration evaluation, the image size of all data sets is 512×512 . For comparison, we choose the Demon algorithm [21] and a B-spline method based on Residual Complexity (RC) [22], which are two state-of-the-art non-rigid registration methods for spatially-varying intensity.

1) *Synthetic data:* For synthetic data, we choose 8 wing pouch images as reference images. An independent experiment is conducted with each reference image. Specifically, for a reference image R , we generate 20 source images, S_1, S_2, \dots, S_{20} , by adding geometric and intensity distortions, to simulate an image sequence with undergoing movement and Ca^{2+} signaling. Let S_i^0 be the result of adding geometric distortion onto R , where S_i is the result of adding random intensity distortion onto S_i^0 . (Details of distortions will be given below.) Our goal is to find a transformation T_i for each S_i ($i = 1, \dots, 20$) and register S_i to R sequentially. To quantify the performance, we compare the registration results between the reference image R and each clean registered image, where a clean registered image is obtained by applying transformation T_i to S_i^0 . The idea is to evaluate whether the registration algorithm is able to find an optimal geometric transformation

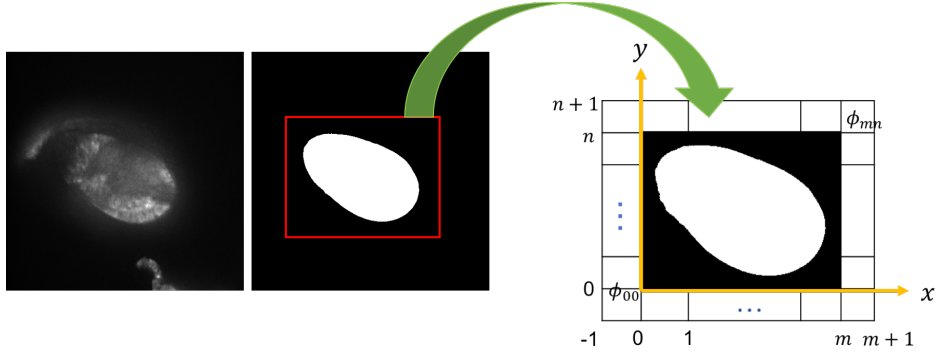


Fig. 7: The configuration of the lattice grid Φ for non-rigid transformation.

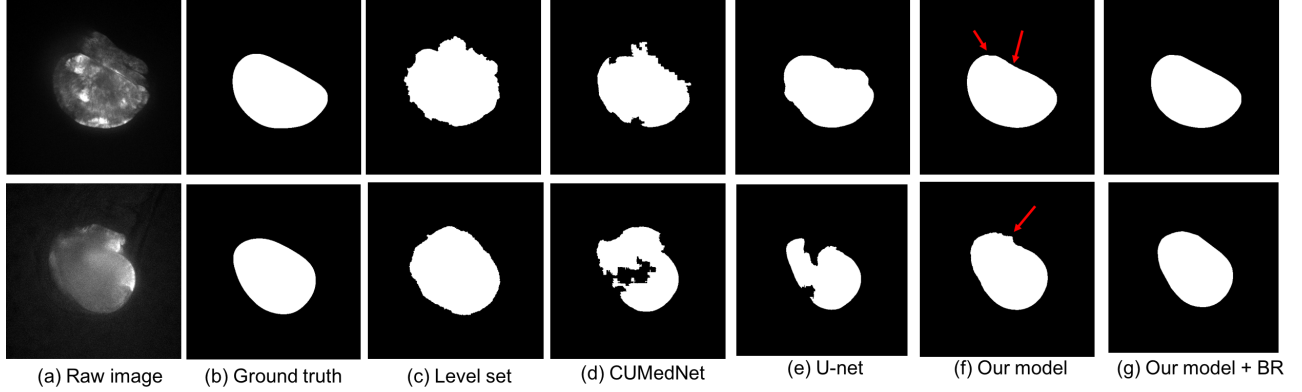


Fig. 8: Segmentation results of different methods on somewhat difficult pouch images (BR = Boundary Refinement). The red arrows indicate locations that can demonstrate the effect of BR.

without damaging the texture inside the wing pouch, as a simulation for evaluating whether the registration algorithm can effectively compensate the movement and growth of the wing pouch even when the intensity profile of the wing pouch undergoes substantial changes due to Ca^{2+} signaling.

For geometric distortions, we apply an elastic spline deformation to perturb the points according to the grid deformation and a rigid transformation (random rotation between 0 to 30 degree and random translation within the image). The spacing between control points in the grid is 32 pixels. For intensity distortion, we take three steps: (1) rescale the image intensity to [0, 0.8]; (ii) add random disk-shaped noise (see Fig. 9) to simulate signal waves; (iii) rescale the image intensity to [0, 1]. Fig. 9 shows a typical synthetic image example.

The intensity root mean square error (RMSE) is selected as the metric, which is frequently used for calculating value variability. RMSE is defined as:

$$RMSE = \sqrt{\frac{\sum_{t=1}^n (y_t - y'_t)^2}{n}}$$

where y_t and y'_t are the intensity values of the reference image and the clean registered image, respectively.

Fig. 11 shows some visual results of different methods, and

Table. II gives quantitative results. The results of our approach are more accurate. Demon has poor performance when the source images have obvious offsets. The RC similarity measure does not yield correct results when the intensity changes a lot. For the 5th and 7th movies in our testing set, the overall intensities of the reference images are relatively low, which means that the rescaling step does not influence them much. Hence in this situation, the RC similarity measure can yield relatively good performance. But, in real wing pouch sequences, intensity change is not priorly known. Our method obtains accurate results with relatively stable performance.

Movie No.	Our method RMSE (pixel)	RC RMSE (pixel)	Demon RMSE (pixel)
1	0.0973 ± 0.0185	0.1368 ± 0.0386	0.1501 ± 0.0226
2	0.0973 ± 0.0211	0.1325 ± 0.0250	0.1835 ± 0.0427
3	0.0913 ± 0.0120	0.1366 ± 0.0328	0.1619 ± 0.0211
4	0.0984 ± 0.0089	0.1191 ± 0.0239	0.1283 ± 0.0180
5	0.0863 ± 0.0108	0.0935 ± 0.0203	0.1239 ± 0.0104
6	0.0876 ± 0.0131	0.1323 ± 0.0589	0.1492 ± 0.0151
7	0.0953 ± 0.0187	0.0960 ± 0.0130	0.1334 ± 0.0206
8	0.0994 ± 0.0197	0.1092 ± 0.0185	0.1748 ± 0.0343
Average	0.0941 ± 0.0154	0.1195 ± 0.0289	0.1506 ± 0.0231

TABLE II: Registration results of synthetic data.

2) *Wing pouch data*: Wing pouch images are quite challenging to register, due to very large intensity oscillation including ROI movements and deformations. Most of the multimodal non-rigid registration methods fail on this problem.

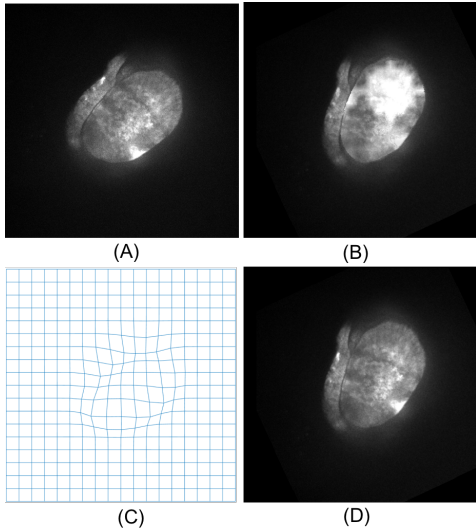


Fig. 9: Illustrating synthetic data. (A) A raw image. (B) A generated synthetic image. (C) The elastic spline deformation used for geometric distortion. (D) The clean registered image, i.e., the result of applying geometric distortion in (C) to the raw image in (A), without any intensity distortion.

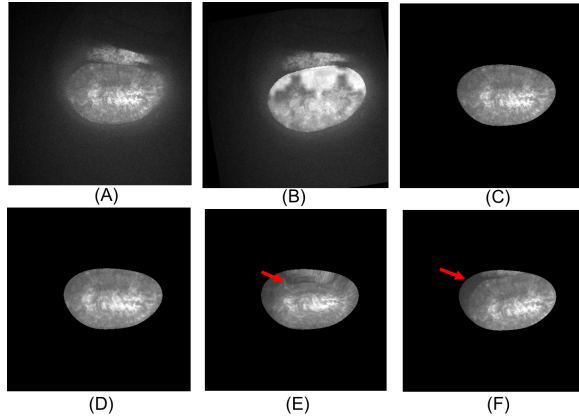


Fig. 10: Sample registration results of synthetic data. (A) A reference image. (B) A source image. (C) The expected registration result. (D) Our method. (E) RC. (F) Demon. The red arrows point to some areas with unsatisfactory registration.

Movie No.	Our method average HD (pixel)	RC average HD (pixel)	Demon average HD (pixel)
1	5.1998 ± 0.4842	5.4901 ± 0.8764	5.6332 ± 0.5171
2	5.5557 ± 1.2502	6.1892 ± 0.8326	6.8185 ± 1.1934
3	5.5678 ± 0.7016	6.4031 ± 0.8118	6.1644 ± 0.5136
4	4.3419 ± 1.3470	6.1602 ± 1.3111	6.7613 ± 0.7866
5	4.6222 ± 0.6843	5.4609 ± 0.8236	5.0719 ± 0.3303
6	4.9131 ± 0.5270	5.3283 ± 1.3936	6.6962 ± 0.7029
7	6.8822 ± 1.1617	7.4133 ± 0.5737	7.1923 ± 0.8363
8	5.3436 ± 0.4430	6.1727 ± 0.8049	5.8454 ± 0.5757
Average	5.3033 ± 0.8249	6.0772 ± 0.9285	6.2729 ± 0.6820

TABLE III: Registration results of real wing pouches.

We randomly choose 8 movies from 150 control videos that were collected under the same experimental and imaging con-

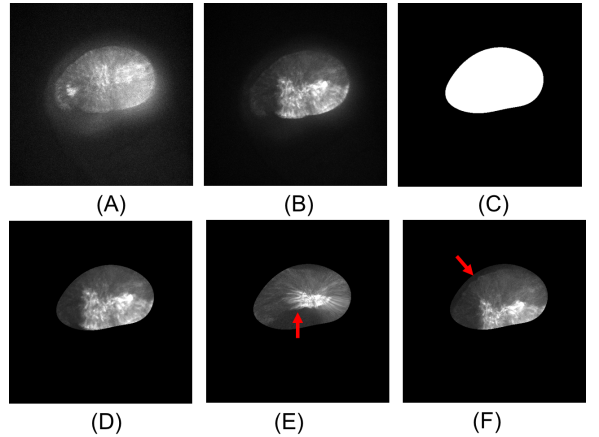


Fig. 11: Registration of real pouches. (A) A reference image. (B) A source image. (C) Intermediate segmentation. (D) Our method. (E) RC (a red arrow points to a distortion part). (F) Demon (a red arrow points to an incorrect alignment position).

ditions. In each movie, we take the first frame as the reference image, and all the other frames as source images. For each movie, we let m_1 denote the reference image, and m_t ($t = 2, \dots, n$) be the source images. Let g_t be the annotation of m_t ($t = 1, \dots, n$). Our goal is to find a transformation T_t for every m_t ($t = 2, \dots, n$) and register m_t to m_1 . To validate the registration results, we apply transformation T_t to g_t ($t = 2, \dots, n$) to obtain the registered annotation boundary and compare the results using the Hausdorff distance (HD) error metric. Let $A = \{a_1, a_2, \dots, a_n\}$, $B = \{b_1, b_2, \dots, b_n\}$, where a_i and b_i represent the boundaries of registered annotations. We define: $HD = \max(\max_i \{d(a_i, B)\}, \max_j \{d(b_j, A)\})$, where $d(a_i, B) = \min_j \|b_j - a_i\|$.

Table III gives the quantitative results. Our approach achieves accurate boundary shapes in registering wing pouch sequences. Also, our method obtains clear texture inside ROIs, as shown by the examples in Fig. 11. RC may severely damage the texture, and thus may damage Ca^{2+} signaling patterns. Demon can maintain better texture than RC, but it may align source images to incorrect positions.

We also evaluate the algorithm used in our mapping stage and compare with other methods for finding optimal transformation. First, we process the source images through the segmentation stage and the rigid transformation step. Then, we perform non-rigid registration using different methods. Our method achieves accurate results. Fig. 12 shows the mapping performance of different methods. It is evident that our method yields better performance. RC still suffers a distortion issue. Demon may also have distorted texture and may align the source to the incorrect position when the shapes in two images differ considerably.

IV. DISCUSSIONS AND CONCLUSIONS

In this paper, we propose a new two-stage non-rigid registration approach for wing pouch image sequence analysis. Our approach first segments wing pouches in image frames using a deep learning (FCN) model and a graph search algorithm, and

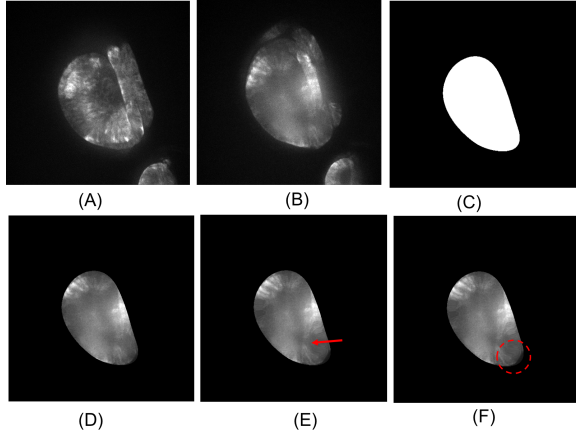


Fig. 12: Mapping performance based on the same segmentation. (A) A reference image. (B) A source image. (C) Intermediate segmentation. (D) Our method. (E) RC (a red arrow points to a distortion part). (F) Demon (a red circle marks an incorrect alignment position).

utilizes the segmentation to compute an optimal transformation to register the image sequences frame by frame. Comparing to the state-of-the-art non-rigid methods for biomedical image registration, our approach achieves higher accuracy in aligning images with non-negligible texture distortion. Our method lays a foundation for quantitative analysis of wing pouch image sequences in the studies of Ca^{2+} signaling related diseases.

Our approach may be extended to other biomedical image registration problems, especially when the intensity profiles and texture patterns of the target objects suffer significant changes. The mapping stage is application-dependent, while the segmentation stage is general and adaptable. Our FCN model can be adapted to or re-trained for different problems and the parameters of the graph search algorithm can be tuned based on the shape and prior knowledge of the problems.

ACKNOWLEDGMENT

This research was supported in part by the Nanoelectronics Research Corporation (NERC), a wholly-owned subsidiary of the Semiconductor Research Corporation (SRC), through Extremely Energy Efficient Collective Electronics (EXCEL), an SRC-NRI Nanoelectronics Research Initiative under Research Task ID 2698.005. The research was also supported in part by NSF grants CCF-1640081, CCF-1217906, CNS-1629914, CCF-1617735, CBET-1403887, and CBET-1553826, Notre Dame Advanced Diagnostics and Therapeutics and Harper Cancer Research Institute Research like a Champion awards, Walther Cancer Foundation Interdisciplinary Interface Training Project, the Notre Dame Advanced Diagnostics and Therapeutics Berry Fellowship, the Notre Dame Integrated Imaging Facility, the Bloomington Stock Center for fly stocks, and the Developmental Studies Hybridoma Bank for antibodies.

REFERENCES

- [1] Q. Wu, P. Brodskiy, C. Narciso, M. Levis, J. Chen, P. Liang, N. Arredondo-Walsh, D. Z. Chen, and J. J. Zartman, “Intercellular calcium waves are controlled by morphogen signaling during organ development,” *bioRxiv*, no. 104745, 2017.
- [2] J. Zartman, S. Restrepo, and K. Basler, “A high-throughput template for optimizing drosophila organ culture with response-surface methods,” *Development*, vol. 140, p. 667674, 2013.
- [3] K. V. Kuchibhotla, C. R. Lattarulo, B. T. Hyman, and B. J. Bacskai, “Synchronous hyperactivity and intercellular calcium waves in astrocytes in Alzheimer mice,” *Science*, vol. 323, no. 5918, pp. 1211–1215, 2009.
- [4] F. M. Davis, I. Azimi, R. A. Faville, A. A. Peters, K. Jalink, J. W. Putney Jr, G. J. Goodhill, E. W. Thompson, S. J. Roberts-Thomson, and G. R. Monteith, “Induction of epithelial-mesenchymal transition (emt) in breast cancer cells is calcium signal dependent,” *Oncogene*, vol. 33, no. 18, p. 2307, 2014.
- [5] A. Roche, G. Malandain, and N. Ayache, “Unifying maximum likelihood approaches in medical image registration,” *Int. J. Imaging Syst. Technol.*, vol. 11, p. 7180, 2000.
- [6] F. Maes, D. Vandermeulen, and P. Suetens, “Medical image registration using mutual information,” *Proceedings of the IEEE*, vol. 91, no. 10, pp. 1699–1722, 2003.
- [7] A. Wong and J. Orchard, “Robust multimodal registration using local phase-coherence representations,” *Journal of Signal Processing Systems*, vol. 54, no. 1-3, p. 89, 2009.
- [8] A. El-Baz, A. Farag, G. Gimel’farb, and A. E. Abdel-Hakim, “Image alignment using learning prior appearance model,” in *Image Processing, 2006 IEEE International Conference on*, 2006, pp. 341–344.
- [9] J. Woo, M. Stone, and J. L. Prince, “Multimodal registration via mutual information incorporating geometric and spatial context,” *IEEE Transactions on Image Processing*, vol. 24, no. 2, pp. 757–769, 2015.
- [10] L. Yang, Y. Zhang, J. Chen, S. Zhang, and D. Z. Chen, “Suggestive annotation: A deep active learning framework for biomedical image segmentation,” *arXiv preprint arXiv:1706.04737*, 2017.
- [11] J. Long, E. Shelhamer, and T. Darrell, “Fully convolutional networks for semantic segmentation,” in *Proceedings of the IEEE Conference on Computer Vision and Pattern Recognition*, 2015, pp. 3431–3440.
- [12] H. Chen, X. Qi, J.-Z. Cheng, P.-A. Heng *et al.*, “Deep contextual networks for neuronal structure segmentation,” in *AAAI*, 2016, pp. 1167–1173.
- [13] J. Chen, L. Yang, Y. Zhang, M. Alber, and D. Z. Chen, “Combining fully convolutional and recurrent neural networks for 3D biomedical image segmentation,” in *Advances in Neural Information Processing Systems*, 2016, pp. 3036–3044.
- [14] O. Ronneberger, P. Fischer, and T. Brox, “U-net: Convolutional networks for biomedical image segmentation,” in *Int. Conf. Medical Image Computing and Computer-Assisted Intervention*, 2015, pp. 234–241.
- [15] J. Schindelin, I. Arganda-Carreras, E. Frise, V. Kaynig, M. Longair, T. Pietzsch, S. Preibisch, C. Rueden, S. Saalfeld, B. Schmid *et al.*, “Fiji: an open-source platform for biological-image analysis,” *Nature Methods*, vol. 9, no. 7, pp. 676–682, 2012.
- [16] S. Lee, G. Wolberg, K.-Y. Chwa, and S. Y. Shin, “Image metamorphosis with scattered feature constraints,” *IEEE Transactions on Visualization and Computer Graphics*, vol. 2, no. 4, pp. 337–354, 1996.
- [17] S. Klein, M. Staring, and J. P. Pluim, “Evaluation of optimization methods for nonrigid medical image registration using mutual information and b-splines,” *IEEE Transactions on Image Processing*, vol. 16, no. 12, pp. 2879–2890, 2007.
- [18] D. Rueckert, L. Sonoda, E. Denton, S. Rankin, C. Hayes, M. O. Leach, D. Hill, and D. J. Hawkes, “Comparison and evaluation of rigid and non-rigid registration of breast MR images,” in *SPIE*, vol. 3661, 1999, pp. 78–88.
- [19] C. Li, C.-Y. Kao, J. C. Gore, and Z. Ding, “Minimization of region-scalable fitting energy for image segmentation,” *IEEE Transactions on Image Processing*, vol. 17, no. 10, pp. 1940–1949, 2008.
- [20] D. Kingma and J. Ba, “Adam: A method for stochastic optimization,” *arXiv preprint arXiv:1412.6980*, 2014.
- [21] D.-J. Kroon and C. H. Slump, “MRI modality transformation in demon registration,” in *Biomedical Imaging: From Nano to Macro, IEEE International Symposium on*, 2009, pp. 963–966.
- [22] A. Myronenko and X. Song, “Image registration by minimization of residual complexity,” in *Computer Vision and Pattern Recognition, IEEE Conference on*, 2009, pp. 49–56.